Defect-free model of amorphous silicon with pristine electronic structure

Louise A. M. Rosset [1], Chinonso Ugwumadu [2], Stephen R. Elliott [3], David A. Drabold [4] and Volker L. Deringer [1,*]

[1] *Inorganic Chemistry Laboratory, Department of Chemistry, University of Oxford, Oxford, United Kingdom*

[2] *Quantum and Condensed Matter Physics (T-4) Group, Los Alamos National Laboratory, Los Alamos, New Mexico 87544-7113, USA*

[3] *Physical and Theoretical Chemistry Laboratory, Department of Chemistry, University of Oxford, Oxford, United Kingdom*

[4] *Department of Physics and Astronomy, Ohio University, Athens, Ohio 45701, USA*

(Received 2 July 2026; accepted 25 August 2026; published 4 November 2026)

Amorphous silicon (*a*-Si) is understood to be a canonical continuous random network material, ideally defined by fully fourfold coordination. Here, we show that a defect-free ("ideal") model of *a*-Si from machine-learning-driven molecular-dynamics simulations [Rosset *et al.*, Nat. Commun. **16**, 2360 (2025)], subsequently evaluated with hybrid-level density-functional theory computations, can accurately reproduce the experimentally observed electronic band gap. We compare this model with one resulting from the Wooten-Winer-Weaire bond-switching approach and with other recent approximants to ideal *a*-Si. More broadly, our work provides a platform for studies of band tails, optical properties, and transport in *a*-Si.

DOI: 10.1103/cvf3-cd4p

Amorphous silicon (*a*-Si) has long been thought of as a continuous random network (CRN) material [1], with fourfold coordination ($N = 4$ for all atoms) but without long-range structural order. The CRN model is an idealized picture that approximates the experimental reality, in which coordination defects ($N \neq 4$) are unavoidable [2], yet it is central to our fundamental understanding of disordered networks. Approaching the defect-free limit is relevant for precision instruments such as LIGO gravitational-wave detectors that rely on hydrogen-free *a*-Si for its low mechanical loss and correspondingly significant reduction in thermal noise [3].

Computationally, the CRN is often approximated using the Wooten-Winer-Weaire (WWW) bond-switching algorithm: starting from a crystalline (*c*-) Si structure, second-neighbor bonds are rearranged to change the network topology, while constraining it to $N = 4$ throughout [4]. Other protocols do not enforce fourfold coordination, such that almost all reported defect-free *a*-Si models have been generated with the WWW protocol [5].

Despite the existence of several defect-free structural models, to the authors' knowledge, none has succeeded in demonstrating quantitative agreement with the experimental band gap of *a*-Si, which varies between 1.5 and 1.8 eV, depending on the preparation method [6]. This is often due to localized states at tails of the valence- and conduction-band edges, thus reducing the electronic gap. Previous studies have focused on the effect of hydrogenation on cleaning up the midgap states by saturating dangling bonds and reducing network strain, thereby modifying the band tails and opening up the band gap [7–9]. An ideal, defect-free network would not require hydrogenation, instead presenting a "clean" electronic gap.

We recently created a large dataset of *a*-Si structures from a series of melt-quench molecular-dynamics simulations [10], driven by an efficient machine-learning-based interatomic potential (MLIP) [11,12], systematically sampling the configurational space of *a*-Si by varying the mass density and quench rate. From this library of thousands of disordered structures, we discovered a defect-free 216-atom model quenched at a rate of 10^{10} K/s, denoted as Rosset-10 in the following. We note that no coordination criterion was imposed during the simulation, so the system was not constrained to be defect free, unlike in the WWW protocol. The generation of a defect-free *a*-Si network by melt quenching is therefore a rare and stochastic event, and requires a large number of attempts, which can be accelerated using MLIPs [10,13].

In this paper, we characterize the electronic structure of our Rosset-10 structural model of *a*-Si, and show that it faithfully reproduces the value of the electronic band gap from experiment. We compare it to three existing high-quality models of *a*-Si (Table I): (i) WWW-216, obtained from the WWW protocol [4] paired with the Keating potential [18]. Its electronic structure has been characterized previously [15,19]; (ii) Pedersen-Y, obtained from a set of density-functional theory (DFT) annealing, relaxation, and rescaling procedures [16]. While this structure is not entirely defect free (Table I), it agrees very well with various experimental measurements of short- and medium-range structural order; (iii) Zongo-R2, generated by the Activation Relaxation Technique nouveau (ARTn), which moves the system along the potential-energy surface by searching for first-order saddle points, coupled with an MLIP [5]. It is the only other defect-free 216-atom model that was not generated with the WWW protocol. We note that Table I is not an exhaustive survey of simulation protocols for *a*-Si: others exist, such as Monte Carlo [20] or hybrid approaches [21–23].

*Contact author: volker.deringer@chem.ox.ac.uk

Published by the American Physical Society under the terms of the Creative Commons Attribution 4.0 International license. Further distribution of this work must maintain attribution to the author(s) and the published article's title, journal citation, and DOI.

TABLE I. Summary of the relaxed *a*-Si models discussed in the present study, detailing the following: generation protocol; number of atoms and percentage of fourfold coordinated ones; mass density; porosity; percentage of locally crystal-like environments by Polyhedral Template Matching (PTM) and Common Neighbor Analysis (CNA); structural similarity to cubic diamond-type Si (*c*-Si) calculated using the SOAP kernel [14]; and energy relative to *c*-Si as predicted by HSE06-level DFT computations.

Sample	Protocol	No. of atoms	Fourfold coord. (%)	Density (g/cm^3)	Porosity (%)	PTM (%)	CNA (%)	SOAP sim.	ΔE (eV/at.)
WWW-216 [15]	WWW bond switching [4]	216	100	2.304	0.31	0	7.9	0.895	0.196
Pedersen-Y [16]	DFT relaxations	215	98.1	2.267	0.22	0	0	0.911	0.189
Zongo-R2 [5]	ARTn runs [17]	216	100	2.256	0.24	0.5	19.9	0.919	0.160
Rosset-10 [10]	Melt quench, 10^{10} K/s rate	216	100	2.223	0.28	0	0	0.910	0.138

We employed hybrid-level DFT computations, known to reproduce the experimental band gap of *c*-Si [24,25], and previously used for *a*-Si [26,27]. Computations were carried out using a plane-wave energy cutoff of 540 eV and the projector augmented-wave formalism [28], as implemented in VASP [29,30]. To evaluate all models on an equal footing, we first relaxed each model using the Heyd-Scuseria-Ernzerhof (HSE06) functional [31,32] at the Γ point only. We then computed electronic properties using a Γ-centered *k*-point grid of $2 \times 2 \times 2$ with the HSE06 functional. Further details are available in the Supplemental Material [13] (which includes Refs. [33–45]).

A common first criterion in validating a candidate amorphous structure is the predicted mass density. The density of *a*-Si thin films is estimated around 2.28 g/cm^3 from ion-implanted samples [2,46,47]. The Pedersen-Y model is the closest to this value, likely since volume scaling was included in the generation protocol, but the other models fall within 1%–3% of the experimental value. The porosity is estimated using a fine three-dimensional (3D) mesh and counting empty grid elements with a script developed in the context of Ref. [48]. All models present low porosities, agreeing with reports that pores in *a*-Si are deposition artifacts [49] and should not occur in simulated quenched structures [50]. The higher porosity of the WWW-216 model arises from $m > 8$ rings (Supplemental Material [13]).

To ascertain the CRN nature of the models, we probe the existence of local ordering and compare three common indicators, viz., Polyhedral Template Matching (PTM) [51], Common Neighbor Analysis (CNA) [52–55], and the averaged SOAP kernel similarity [14] to diamond-type (**dia**) Si, where 1 is identical. CNA appears more sensitive than PTM, indicating crystallinity in both the WWW-216 and Zongo-R2 models, while PTM only detects ordering in the latter. This crystallinity is consistent with reports of ordering in the original study [5]. In SOAP terms, the Zongo-R2 model is closest to **dia**, whereas WWW-216 is most dissimilar. Rosset-10 shows no apparent crystallinity and an average SOAP similarity to **dia** relative to the other models and the literature [10,56]. Beyond global structural characteristics, the Supplemental Material includes metrics of short- and medium-range order (Supplemental Material [13]).

The four models show large variations in their energies relative to **dia**, as computed with HSE06. In particular, the Rosset-10 model has the lowest energy among the four. We have previously shown that paracrystalline models have lower energies on average than fully disordered networks [10]; hence this lower energy could reflect crystalline ordering that was not captured by PTM, CNA, or SOAP. Yet, the Rosset-10 model provides excellent agreement with the calorimetrically determined enthalpy of crystallization of $\Delta H = 0.142 \pm 0.003$ eV/atom obtained from ion-implanted samples [57]. Importantly, this means that only the Rosset-10 model fulfills the energy criterion set out in Ref. [58], that requires the energy of a candidate ideal *a*-Si model to fall within the range of 0.07 to 0.15 eV/atom above that of **dia**.

We now turn to the electronic densities of states (DOS), plotted in Fig. 1(a). The shape of the DOS is well reproduced throughout, with the 3*s* orbitals mainly contributing in the −15 to −5 eV range, and the 3*p* orbitals between −5 and 0 eV [61]. The relative heights of the valence-band (VB) and conduction-band (CB) maxima are similar and agree well with previous literature [62,63]. All three defect-free structures have clean band gaps free of midgap states, while the DOS of the Pedersen-Y model does have such states, associated with the aforementioned coordination defects (Table I).

Other important features of the DOS are the exponential tails at the VB and CB edges, known as Urbach tails [64], which have been resolved experimentally [65]. These tails have been linked to atomic filaments, whose electron eigenstates form interconnected clusters of charge [63], and also to topological filaments associated with bond stretching and bending [19,66]. The WWW-216 and Zongo-R2 models show large tails at their CB and VB edges, respectively, while the Rosset-10 model shows small and narrower VB and CB tails.

We report the estimated values of the electronic band gap, E_{gap}, in Fig. 1(b), defined as the difference in energy between the lowest occupied CB (LUMO) state and the highest occupied VB (HOMO) state. For the Pedersen-Y model, we exclude the localized midgap states when defining the band gap. There is a large variation in the estimated E_{gap} values between models, directly reflecting the differences in the Urbach tails. Previously reported values for *a*-Si in the computational literature range between 0.8 and 1.35 eV [67,68]; the WWW-216, Pedersen-Y, and Zongo-R2 models are consistent with these. The Rosset-10 model has a substantially larger E_{gap}, which provides excellent and unprecedented agreement with the experimentally reported range of optical band gaps of *a*-Si, typically between 1.5 and 1.8 eV [6,13,69–71]. We note that our results are obtained from computations with a $2 \times 2 \times 2$ *k*-point grid, and that the estimated E_{gap} varies with *k* sampling and the associated dispersion in the supercell [72,73]. Identical calculations at the Γ point result in gaps that are

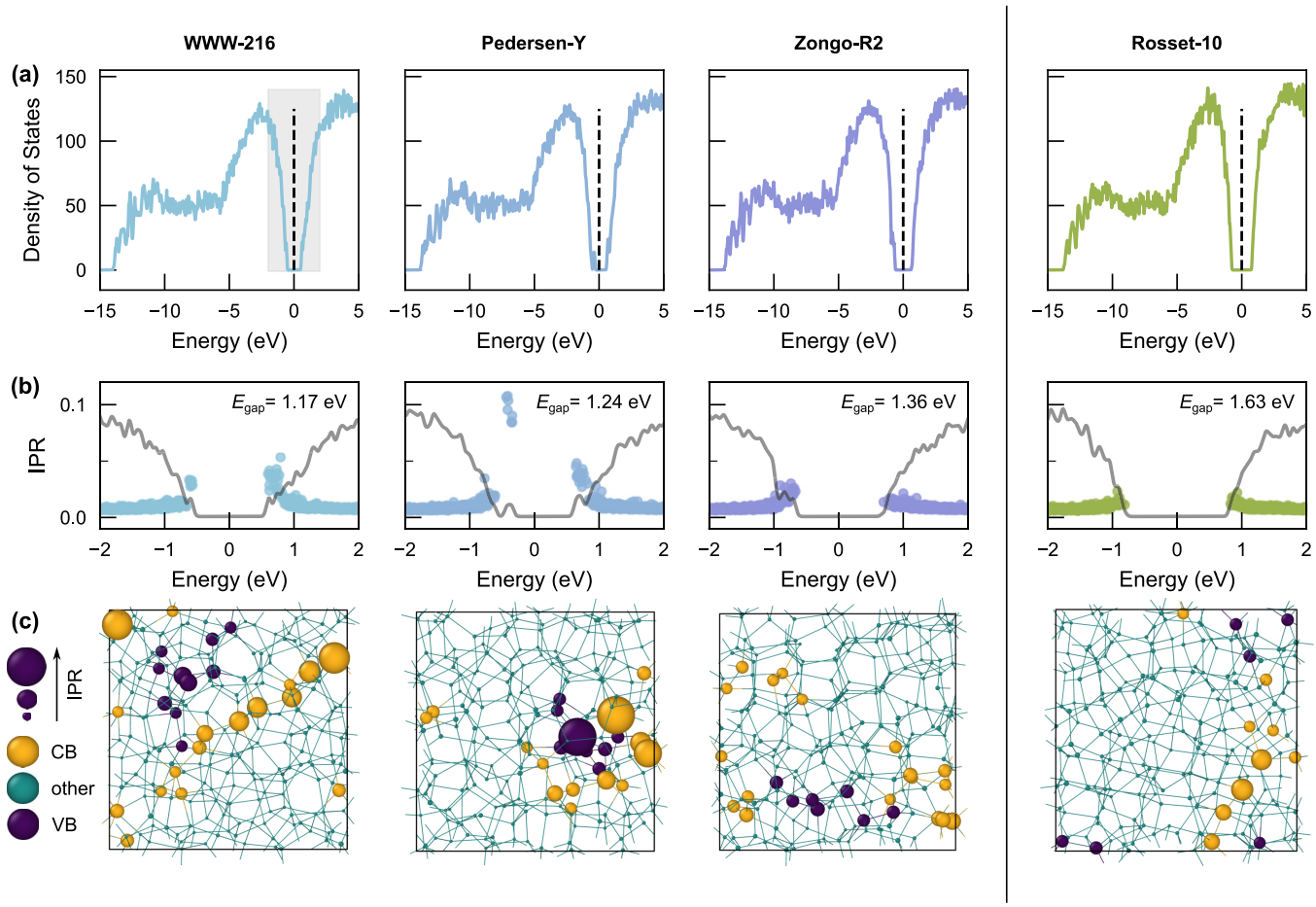


FIG. 1. Electronic structure. (a) Electronic densities of states of the four structural model considered in this study, where a dashed vertical line indicates the Fermi level (E_F) defined as the middle of the gap and centered at 0 eV. Enlarged plots are available in the Supplemental Material [13]. (b) Inverse Participation Ratio (IPR) plots in the region of the band gap for each model, as shaded in gray for the WWW-216 model. The IPR is evaluated for each band and k-point pair; the thick gray line overlays show the densities of states. The quoted E_{gap} value refers to the energy difference between the lowest occupied conduction-band (LUMO) state and the highest occupied valence-band (HOMO) state, omitting the midgap states for the Pedersen-Y model. (c) Visualizations of the spatial localization of the highest IPR sites for each structure using OVITO [59], where atoms are color coded by their IPR contribution to the VB, CB, or other as purple, yellow, or teal, respectively. The atomic radii are scaled proportionally to the relative IPR magnitudes, normalized against the largest IPR contribution across all structural models. A similar analysis of the WWW-216 model, albeit not at the hybrid DFT level, is carried out in Ref. [60].

systematically larger, by 0.02–0.12 eV, giving $E_{gap} = 1.71$ eV for Rosset-10.

To probe these variations in the electronic structure, we focus on the spatial localization of states around the Fermi level, E_F, in Fig. 1(b), plotting the DOS together with inverse participation ratio (IPR) values [74],

$$\mathrm{IPR}_{nk} = \frac{\Sigma_a |c_{nka}|^4}{(\Sigma_a |c_{nka}|^2)^2},$$

where n is the band index, k is the k-point index, a is the atomic orbital, and c is the wave-function coefficient, as calculated with PyProcar [75,76]. The IPR measures how localized or extended the electron states are [63,67]: low values ($\to 0$) correspond to delocalized or extended states that are distributed across the structure, while high values ($\to 1$) correspond to spatially localized states. However, it should be noted that it is not possible to distinguish unambiguously between delocalized and weakly localized states when the localization length is comparable to the simulation-box size, here ≈15 Å, and that size effects from the small model size of 216 atoms may affect the observed electronic properties.

The Pedersen-Y model has highly localized states adjacent to the VB edge, arising from the dangling-bond defect. It also displays some localization at the CB edge, associated with a broader conduction-band tail. The WWW-216 and Zongo-R2 models reveal appreciable localization at the CB edge and the VB edge, respectively. The Rosset-10 model exhibits no significant electron localization, instead seemingly having fully extended (delocalized) states throughout both the VB and CB edges. It appears that the degree of localization around the band gap is inversely correlated with the width of the gap: the models with the smallest E_{gap} values, i.e., WWW-216 and Pedersen-Y, show the most tail localization, while the Rosset-10 model shows no localization and has the largest band gap.

The width of the band gap and the degree of localization are associated with the degree of structural disorder and the presence of coordination defects, respectively

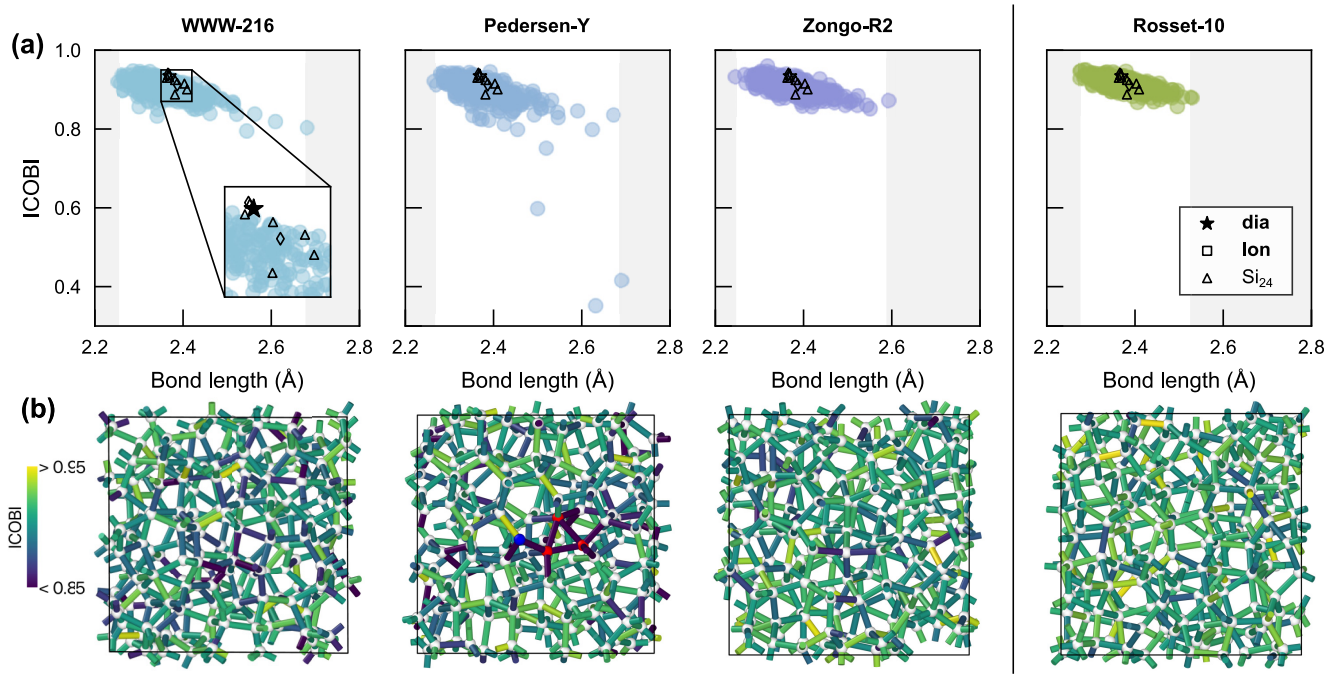


FIG. 2. Chemical bonding. (a) Scatter plots of integrated pairwise crystal orbital bond index ($ICOBI^{(2)}$) values against bond lengths, where gray shading shows the edges of the bond-length distributions. An inset highlights relevant *c*-Si modifications: cubic diamond-type ("**dia**"; star), hexagonal diamond-type ("**lon**"; square) and the open-framework structure of Ref. [84] ("Si_{24}"; triangle). (b) Structure visualizations of the models using OVITO [59], where atoms are color coded by coordination (blue/white/red for three/four/fivefold coordination, respectively), and bonds are color coded by ICOBI value.

[77]. To examine the spatial character of the localized states, Fig. 1(c) shows the atomic regions contributing most strongly to the IPR for states near the band edges, where the atomic radii are scaled proportionally to the largest IPR contribution in the structure. The WWW-216 and Pedersen-Y models exhibit localization on relatively small groups of atoms, arranged in compact clusters. This is consistent with the larger IPR values observed for these models, as higher IPR indicates stronger confinement of the electronic state to a small number of sites [77]. By contrast, the Zongo-R2 and Rosset-10 models show lower IPR values at the band edges and correspondingly more spatially extended localization patterns, which appear as interconnected chains within the network. This behavior is consistent with earlier studies showing that band-tail states in *a*-Si arise from chains of distorted bonds rather than isolated pointlike defects [66,77–79]. In particular, mildly short bonds contribute predominantly to VB tail states, while mildly long bonds contribute predominantly to CB tail states, a trend that is reproduced by the Pedersen-Y and Rosset-10 models, as shown in the Supplemental Material [13].

We turn to the chemical bonding in these structures to understand the large variation in E_{gap} and the exceptionally extended states in the Rosset-10 model. In Fig. 2(a), we plot the integrated crystal orbital bond index ($ICOBI^{(2)}$), obtained with LOBSTER [13,80–82]. $ICOBI^{(2)}$ quantifies the pairwise bond order, such that strong covalent bonds have a value close to 1 [82]. Stretched bonds in the WWW-216 and Pedersen-Y models result in lower ICOBI values, but there are strong outliers in Pedersen-Y falling beyond the exponential bond-length–bond-strength relationship [83]. The distributions for the Zongo-R2 and Rosset-10 models are qualitatively similar, but the bond-length distribution of the latter is narrower, resulting in a more compact scatter. For comparison, an inset shows ICOBI values for crystalline allotropes of Si: cubic and hexagonal diamond-type, and an open-framework structure [84].

To resolve the spatial character of bonding, we visualize the structural models in Fig. 2(b), coloring bonds by their ICOBI values. The low values in the Pedersen-Y model arise from a three-membered ring formed by the overcoordinated Si atoms (red). The three long bonds strain their local environment into a larger cluster with disrupted bonding, in turn leading to the localized states in the gap and in the band tails. The bonds around the undercoordinated Si atom (blue) also leads to local strain and higher ICOBI values. In the WWW-216 model, some bonds with low ICOBI values belong to four-membered rings, while others form linear chains, or isolated stretched bonds. Conversely, the ICOBI values are more uniformly distributed in the Zongo-R2 and Rosset-10 models, and the bonds with low ICOBI values do not cluster.

A model of *a*-Si with no localized states, a narrow bond-angle distribution, and low excess energy with respect to **dia** has been hypothesized to represent an *ideal* *a*-Si network [67]. All three criteria are fulfilled with the Rosset-10 model, as shown in Fig. 1, Fig. S2 [13], and Table I. We further propose that an "ideal" *a*-Si model must have a narrow distribution of bond lengths without excessively short nor long bonds, a criterion that appears necessary to achieve an absence of localized states at the VB and CB band edges, respectively.

Looking forward, our model could serve as a platform to further understand the effect of defects and dopants in

a-Si [85], or to make accurate predictions of carrier mobility [86]. These effects are of interest since *a*-Si is used in both intrinsic and doped forms in solar-cell heterojunctions [87]. The model's large band gap may be of interest in studying the optical absorption of *a*-Si, relevant for LIGO applications [3]. Our model could also be used in the future to investigate why *a*-Si has a larger band gap than the indirect gap in **dia**, in an analogous study to the one recently conducted on *c*-Si in Ref. [88]. More broadly, this model of an ideal random network opens avenues for the exploration of the electronic structure of CRN-like disordered materials.

This work was supported by UK Research and Innovation [Grant No. EP/X016188/1]. C.U. acknowledges support from the laboratory directed Research and Development (LDRD) program at Los Alamos National Laboratory (LANL) through a Director's Postdoctoral Fellowship (Project No. 20240877PRD4). S.R.E. is grateful to the Leverhulme Trust (U.K.) for a support from a Fellowship. D.A.D. acknowledges support from the U.S. National Science Foundation (Project No. MRI-2320493). We are grateful for computational support from the U.K. national high performance computing service, ARCHER2 (see also Ref. [89]), for which access was obtained via the UKCP consortium and funded by EPSRC Grant Ref. EP/X035891/1.

DATA AVAILABILITY

Data supporting the findings of this article are publicly available [90].

[1] W. H. Zachariasen, The atomic arrangement in glass, J. Am. Chem. Soc. **54**, 3841 (1932).
[2] K. Laaziri, S. Kycia, S. Roorda, M. Chicoine, J. L. Robertson, J. Wang, and S. C. Moss, High-energy x-ray diffraction study of pure amorphous silicon, Phys. Rev. B **60**, 13520 (1999).
[3] R. Birney, J. Steinlechner, Z. Tornasi, S. MacFoy, D. Vine, A. S. Bell, D. Gibson, J. Hough, S. Rowan, P. Sortais, S. Sproules, S. Tait, I. W. Martin, and S. Reid, Amorphous silicon with extremely low absorption: Beating thermal noise in gravitational astronomy, Phys. Rev. Lett. **121**, 191101 (2018).
[4] F. Wooten, K. Winer, and D. Weaire, Computer generation of structural models of amorphous Si and Ge, Phys. Rev. Lett. **54**, 1392 (1985).
[5] K. Zongo, H. Sun, C. Ouellet-Plamondon, N. Mousseau, and L. K. Béland, Amorphous silicon structures generated using a moment tensor potential and the activation relaxation technique nouveau, Phys. Rev. B **111**, 214209 (2025).
[6] R. H. Klazes, M. H. L. M. van den Broek, J. Bezemer, and S. Radelaar, Determination of the optical bandgap of amorphous silicon, Philos. Mag. B **45**, 377 (1982).
[7] W. Y. Ching, D. J. Lam, and C. C. Lin, Electronic states and bonding configurations in hydrogenated amorphous silicon, Phys. Rev. B **21**, 2378 (1980).
[8] G. Allan, C. Delerue, and M. Lannoo, Electronic structure and localized states in a model amorphous silicon, Phys. Rev. B **57**, 6933 (1998).
[9] R. V. Meidanshahi, S. Bowden, and S. M. Goodnick, Electronic structure and localized states in amorphous Si and hydrogenated amorphous Si, Phys. Chem. Chem. Phys. **21**, 13248 (2019).
[10] L. A. M. Rosset, D. A. Drabold, and V. L. Deringer, Signatures of paracrystallinity in amorphous silicon from machine-learning-driven molecular dynamics, Nat. Commun. **16**, 2360 (2025).
[11] J. D. Morrow and V. L. Deringer, Indirect learning and physically guided validation of interatomic potential models, J. Chem. Phys. **157**, 104105 (2022).
[12] The MLIP model of Ref. [11] was distilled from the Si-GAP-18 potential introduced in Ref. [37].
[13] See Supplemental Material at http://link.aps.org/supplemental/10.1103/cvf3-cd4p for further discussion of the computational methods, and additional results including structural (Sec. S2.1) and electronic characterization (Secs. S2.2-S2.4) of the models.
[14] A. P. Bartók, R. Kondor, and G. Csányi, On representing chemical environments, Phys. Rev. B **87**, 184115 (2013).
[15] B. R. Djordjević, M. F. Thorpe, and F. Wooten, Computer model of tetrahedral amorphous diamond, Phys. Rev. B **52**, 5685 (1995).
[16] A. Pedersen, L. Pizzagalli, and H. Jónsson, Optimal atomic structure of amorphous silicon obtained from density functional theory calculations, New J. Phys. **19**, 063018 (2017).
[17] N. Mousseau, L. K. Béland, P. Brommer, J.-F. Joly, F. El-Mellouhi, E. Machado-Charry, M.-C. Marinica, and P. Pochet, The activation-relaxation technique: ART nouveau and kinetic ART, J. Phys. B: At. Mol. Phys. **2012**, 925278 (2012).
[18] P. N. Keating, Effect of invariance requirements on the elastic strain energy of crystals with application to the diamond structure, Phys. Rev. **145**, 637 (1966).
[19] Y. Pan, M. Zhang, and D. A. Drabold, Topological and topological-electronic correlations in amorphous silicon, J. Non-Cryst. Solids **354**, 3480 (2008).
[20] G. Opletal, T. C. Petersen, I. K. Snook, and D. G. McCulloch, Modeling of structure and porosity in amorphous silicon systems using Monte Carlo methods, J. Chem. Phys. **126**, 214705 (2007).
[21] M. J. Cliffe, M. T. Dove, D. A. Drabold, and A. L. Goodwin, Structure determination of disordered materials from diffraction data, Phys. Rev. Lett. **104**, 125501 (2010).
[22] A. Pandey, P. Biswas, and D. A. Drabold, Inversion of diffraction data for amorphous materials, Sci. Rep. **6**, 33731 (2016).
[23] D. Igram, B. Bhattarai, P. Biswas, and D. A. Drabold, Large and realistic models of amorphous silicon, J. Non-Cryst. Solids **492**, 27 (2018).
[24] J. Heyd, J. E. Peralta, G. E. Scuseria, and R. L. Martin, Energy band gaps and lattice parameters evaluated with the Heyd-Scuseria-Ernzerhof screened hybrid functional, J. Chem. Phys. **123**, 174101 (2005).
[25] H. J. Xiang, B. Huang, E. Kan, S.-H. Wei, and X. G. Gong, Towards direct-gap silicon phases by the inverse band structure design approach, Phys. Rev. Lett. **110**, 118702 (2013).

[26] K. Jarolimek, E. Hazrati, R. A. de Groot, and G. A. de Wijs, Band offsets at the interface between crystalline and amorphous silicon from first principles, Phys. Rev. Appl. **8**, 014026 (2017).

[27] J. D. Morrow, C. Ugwumadu, D. A. Drabold, S. R. Elliott, A. L. Goodwin, and V. L. Deringer, Understanding defects in amorphous silicon with million-atom simulations and machine learning, Angew. Chem. Int. Ed. **63**, e202403842 (2024).

[28] P. E. Blöchl, Projector augmented-wave method, Phys. Rev. B **50**, 17953 (1994).

[29] G. Kresse and J. Furthmüller, Efficient iterative schemes for *ab initio* total-energy calculations using a plane-wave basis set, Phys. Rev. B **54**, 11169 (1996).

[30] G. Kresse and D. Joubert, From ultrasoft pseudopotentials to the projector augmented-wave method, Phys. Rev. B **59**, 1758 (1999).

[31] J. Heyd, G. E. Scuseria, and M. Ernzerhof, Hybrid functionals based on a screened Coulomb potential, J. Chem. Phys. **118**, 8207 (2003).

[32] J. Heyd, G. E. Scuseria, and M. Ernzerhof, Erratum: "Hybrid functionals based on a screened Coulomb potential" [J. Chem. Phys. 118, 8207 (2003)], J. Chem. Phys. **124**, 219906 (2006).

[33] G. Kresse and J. Hafner, *Ab initio* molecular-dynamics simulation of the liquid-metal–amorphous-semiconductor transition in germanium, Phys. Rev. B **49**, 14251 (1994).

[34] G. Kresse and J. Furthmüller, Efficiency of *ab-initio* total energy calculations for metals and semiconductors using a plane-wave basis set, Comput. Mater. Sci. **6**, 15 (1996).

[35] J. R. A. Carlsson, X.-H. Li, S. F. Gong, and H. T. G. Hentzell, Structural and optical band-gap properties of the amorphous semiconducting $Si_{1-x}B_x$ alloy, J. Appl. Phys. **74**, 891 (1993).

[36] A. J. M. Berntsen, W. F. Van der Weg, P. A. Stolk, and F. W. Saris, Separating the effects of hydrogen and bond-angle variation on the amorphous-silicon band gap, Phys. Rev. B **48**, 14656 (1993).

[37] A. P. Bartók, J. Kermode, N. Bernstein, and G. Csányi, Machine learning a general-purpose interatomic potential for silicon, Phys. Rev. X **8**, 041048 (2018).

[38] V. L. Deringer, N. Bernstein, A. P. Bartók, M. J. Cliffe, R. N. Kerber, L. E. Marbella, C. P. Grey, S. R. Elliott, and G. Csányi, Realistic atomistic structure of amorphous siliconfrom machine-learning-driven molecular dynamics, J. Phys. Chem. Lett. **9**, 2879 (2018).

[39] V. L. Deringer, N. Bernstein, G. Csányi, C. Ben Mahmoud, M. Ceriotti, M. Wilson, D. A. Drabold, and S. R. Elliott, Origins of structural and electronic transitions in disordered silicon, Nature **589**, 59 (2021).

[40] J. Fortner and J. S. Lannin, Radial distribution functions of amorphous silicon, Phys. Rev. B **39**, 5527 (1989).

[41] K. Laaziri, S. Kycia, S. Roorda, M. Chicoine, J. L. Robertson, J. Wang, and S. C. Moss, High resolution radial distribution function of pure amorphous silicon, Phys. Rev. Lett. **82**, 3460 (1999).

[42] S. M. Nakhmanson, P. M. Voyles, N. Mousseau, G. T. Barkema, and D. A. Drabold, Realistic models of paracrystalline silicon, Phys. Rev. B **63**, 235207 (2001).

[43] P. Grigorev, L. Frérot, F. Birks, A. Gola, J. Golebiowski, J. Grießer, J. L. Hörmann, A. Klemenz, G. Moras, W. G. Nöhring, J. A. Oldenstaedt, P. Patel, T. Reichenbach, T. Rocke, L. Shenoy, M. Walter, S. Wengert, L. Zhang, J. R. Kermode, and L. Pastewka, Matscipy: Materials science at the atomic scale with Python, J. Open Source Softw. **9**, 5668 (2024).

[44] R. Dronskowski and P. E. Blöchl, Crystal orbital Hamilton populations (COHP): Energy-resolved visualization of chemical bonding in solids based on density-functional calculations, J. Phys. Chem. **97**, 8617 (1993).

[45] V. L. Deringer, A. L. Tchougréeff, and R. Dronskowski, Crystal orbital Hamilton population (COHP) analysis as projected from plane-wave basis sets, J. Phys. Chem. A **115**, 5461 (2011).

[46] J. S. Custer, M. O. Thompson, D. C. Jacobson, J. M. Poate, S. Roorda, W. C. Sinke, and F. Spaepen, Density of amorphous Si, Appl. Phys. Lett. **64**, 437 (1994).

[47] K. Laaziri, S. Roorda, and J. M. Baribeau, Density of amorphous Si_xGe_{1-x} alloys prepared by high-energy ion implantation, J. Non-Cryst. Solids **191**, 193 (1995).

[48] Y. Liu, Y. Zhou, R. Ademuwagun, L. Walterbos, J. George, S. R. Elliott, and V. L. Deringer, Medium-range structural order in amorphous arsenic, J. Am. Chem. Soc. **148**, 9400 (2026).

[49] S. C. Moss and J. F. Graczyk, Evidence of voids within the as-deposited structure of glassy silicon, Phys. Rev. Lett. **23**, 1167 (1969).

[50] L. J. Lewis, Fifty years of amorphous silicon models: The end of the story? J. Non-Cryst. Solids **580**, 121383 (2022).

[51] P. M. Larsen, S. Schmidt, and J. Schiøtz, Robust structural identification via polyhedral template matching, Modelling Simul. Mater. Sci. Eng. **24**, 055007 (2016).

[52] J. D. Honeycutt and H. C. Andersen, Molecular dynamics study of melting and freezing of small Lennard-Jones clusters, J. Phys. Chem. **91**, 4950 (1987).

[53] A. S. Clarke and H. Jónsson, Structural changes accompanying densification of random hard-sphere packings, Phys. Rev. E **47**, 3975 (1993).

[54] A. Stukowski, Structure identification methods for atomistic simulations of crystalline materials, Modelling Simul. Mater. Sci. Eng. **20**, 045021 (2012).

[55] E. Maras, O. Trushin, A. Stukowski, T. Ala-Nissila, and H. Jónsson, Global transition path search for dislocation formation in Ge on Si(001), Comput. Phys. Commun. **205**, 13 (2016).

[56] N. Bernstein, B. Bhattarai, G. Csányi, D. A. Drabold, S. R. Elliott, and V. L. Deringer, Quantifying chemical structure and machine-learned atomic energies in amorphous and liquid silicon, Angew. Chem. Int. Ed. **58**, 7057 (2019).

[57] S. Roorda and L. J. Lewis, Comment on "The local structure of amorphous silicon", Science **338**, 1539 (2012).

[58] D. A. Drabold, Silicon: The gulf between crystalline and amorphous, Phys. Status Solidi RRL **5**, 359 (2011).

[59] A. Stukowski, Visualization and analysis of atomistic simulation data with OVITO–The Open Visualization Tool, Modelling Simul. Mater. Sci. Eng. **18**, 015012 (2010).

[60] C. Ugwumadu, D. A. Drabold, and R. M. Tutchton, Real-space mapping of electronic conductivity in complex materials, arXiv:2606.24914.

[61] Y. Furukawa and Y.-I. Matsushita, Analysis of single and composite structural defects in pure amorphous silicon: A first-principles study, J. Non-Cryst. Solids **473**, 64 (2017).

[62] M. F. Thorpe and D. Weaire, Electronic density of states of amorphous Si and Ge, Phys. Rev. Lett. **27**, 1581 (1971).

[63] J. Dong and D. A. Drabold, Atomistic structure of band-tail states in amorphous silicon, Phys. Rev. Lett. **80**, 1928 (1998).

[64] F. Urbach, The long-wavelength edge of photographic sensitivity and of the electronic absorption of solids, Phys. Rev. **92**, 1324 (1953).

[65] S. Aljishi, J. D. Cohen, S. Jin, and L. Ley, Band tails in hydrogenated amorphous silicon and silicon-germanium alloys, Phys. Rev. Lett. **64**, 2811 (1990).

[66] D. A. Drabold, Y. Li, B. Cai, and M. Zhang, Urbach tails of amorphous silicon, Phys. Rev. B **83**, 045201 (2011).

[67] M. Durandurdu, D. A. Drabold, and N. Mousseau, Approximate *ab initio* calculations of electronic structure of amorphous silicon, Phys. Rev. B **62**, 15307 (2000).

[68] G. T. Barkema and N. Mousseau, High-quality continuous random networks, Phys. Rev. B **62**, 4985 (2000).

[69] G. K. M. Thutupalli and S. G. Tomlin, The optical properties of amorphous and crystalline silicon, J. Phys. C: Solid State Phys. **10**, 467 (1977).

[70] N.-M. Park, C.-J. Choi, T.-Y. Seong, and S.-J. Park, Quantum confinement in amorphous silicon quantum dots embedded in silicon nitride, Phys. Rev. Lett. **86**, 1355 (2001).

[71] C.-C. Huang, Y. Tang, M. van der Laan, J. van de Groep, A. F. Koenderink, and K. Dohnalová, Band-gap tunability in partially amorphous silicon nanoparticles using single-dot correlative microscopy, ACS Appl. Nano Mater. **4**, 288 (2021).

[72] D. A. Drabold, P. A. Fedders, O. F. Sankey, and J. D. Dow, Molecular-dynamics simulations of amorphous Si, Phys. Rev. B **42**, 5135 (1990).

[73] K. Prasai, P. Biswas, and D. A. Drabold, Electrons and phonons in amorphous semiconductors, Semicond. Sci. Technol. **31**, 073002 (2016).

[74] D. J. Thouless, Electrons in disordered systems and the theory of localization, Phys. Rep. **13**, 93 (1974).

[75] U. Herath, P. Tavadze, X. He, E. Bousquet, S. Singh, F. Muñoz, and A. H. Romero, PyProcar: A Python library for electronic structure pre/post-processing, Comput. Phys. Commun. **251**, 107080 (2020).

[76] L. Lang, P. Tavadze, A. Tellez, E. Bousquet, H. Xu, F. Muñoz, N. Vasquez, U. Herath, and A. H. Romero, Expanding PyProcar for new features, maintainability, and reliability, Comput. Phys. Commun. **297**, 109063 (2024).

[77] Y. Pan, F. Inam, M. Zhang, and D. A. Drabold, Atomistic origin of Urbach tails in amorphous silicon, Phys. Rev. Lett. **100**, 206403 (2008).

[78] P. A. Fedders, D. A. Drabold, and S. Nakhmanson, Theoretical study on the nature of band-tail states in amorphous Si, Phys. Rev. B **58**, 15624 (1998).

[79] F. Inam, J. P. Lewis, and D. A. Drabold, Hidden structure in amorphous solids, Phys. Stat. Sol. (a) **207**, 599 (2010).

[80] S. Maintz, V. L. Deringer, A. L. Tchougréeff, and R. Dronskowski, Analytic projection from plane-wave and PAW wavefunctions and application to chemical-bonding analysis in solids, J. Comput. Chem. **34**, 2557 (2013).

[81] R. Nelson, C. Ertural, J. George, V. L. Deringer, G. Hautier, and R. Dronskowski, LOBSTER: Local orbital projections, atomic charges, and chemical-bonding analysis from projector-augmented-wave-based density-functional theory, J. Comput. Chem. **41**, 1931 (2020).

[82] P. C. Müller, C. Ertural, J. Hempelmann, and R. Dronskowski, Crystal orbital bond index: Covalent bond orders in solids, J. Phys. Chem. C **125**, 7959 (2021).

[83] L. Pauling, Atomic radii and interatomic distances in metals, J. Am. Chem. Soc. **69**, 542 (1947).

[84] D. Y. Kim, S. Stefanoski, O. O. Kurakevych, and T. A. Strobel, Synthesis of an open-framework allotrope of silicon, Nat. Mater. **14**, 169 (2015).

[85] K. Winer, I. Hirabayashi, and L. Ley, Exponential conduction-band tail in P-doped *a*-Si:H, Phys. Rev. Lett. **60**, 2697 (1988).

[86] Y. Lee, Y. Hu, D. Kim, S. Datta, and K. Cho, First-principles mobility prediction for amorphous semiconductors, Phys. Rev. B **105**, 085201 (2022).

[87] H. Lin, M. Yang, X. Ru, G. Wang, S. Yin, F. Peng, C. Hong, M. Qu, J. Lu, L. Fang, C. Han, P. Procel, O. Isabella, P. Gao, Z. Li, and X. Xu, Silicon heterojunction solar cells with up to 26.81% efficiency achieved by electrically optimized nanocrystalline-silicon hole contact layers, Nat. Energy **8**, 789 (2023).

[88] E. Oliphant, V. Mantena, M. Brod, G. J. Snyder, and W. Sun, Why does silicon have an indirect band gap? Mater. Horiz. **12**, 3073 (2025).

[89] G. Beckett, J. Beech-Brandt, K. Leach, Z. Payne, A. Simpson, L. Smith, A. Turner, and A. Whiting, ARCHER2 service description, Zenodo, 2024, https://doi.org/10.5281/zenodo.14507040.

[90] L. A. M. Rosset, C. Ugwumadu, S. R. Elliott, D. A. Drabold, and V. L. Deringer, Research data supporting "Defect-free model of amorphous silicon with pristine electronic structure," GitHub, 2026, https://github.com/vldgroup/papers-defect-free-a-si.